Influence of Fermi level pinning on contact potential difference measurements using Kelvin probe force microscopy

Nobuyuki Ishida[1, *]

[1] *National Institute for Materials Science, Tsukuba, Ibaraki 305-0047, Japan*

(Dated: March 5, 2025)

We theoretically investigated the influence of Fermi-level pinning on contact potential difference (CPD) measurements conducted via Kelvin probe force microscopy (KPFM) on semiconductor surfaces. To systematically modulate the strength of the surface pinning, virtual surface states were introduced within the semiconductor bandgap, and the density of states (DOS) was varied. The numerically simulated CPD values varied depending on the DOS of the surface states, reflecting the magnitude of the surface band bending (surface potential). However, we found that under certain conditions, the CPD values obtained by KPFM deviated from the physical quantities directly associated with the surface potential. Our results provide valuable insights for enhancing the accuracy of KPFM data analysis and interpretation.

I. BACKGROUND

Kelvin probe force microscopy (KPFM) is a measurement technique that combines the Kelvin probe (KP) method, originally developed by Lord Kelvin, with atomic force microscopy (AFM) [1, 2]. This method enables local measurement of the contact potential difference (CPD) and has been widely used to characterize various electronic [3–9] and ionic devices [10–15]. The CPD, also known as the Volta potential difference, is defined as the electric potential difference between one point in vacuum close to the surface of M1 and another point in vacuum close to the surface of M2, where M1 and M2 are two uncharged metals brought into contact [16]. This value corresponds to the difference between the work functions of the two metals. In this study, we denote the work function difference between the probe tip and sample as V_{CPD}.

In KPFM or KP measurements, the CPD is detected by identifying the bias voltage (U^*) at which the electrostatic force or displacement current between the probe and sample is minimized. KPFM and KP measurements of pristine metal surfaces using a well-defined metal probe yield U^* equivalent to V_{CPD} [17, 18]. However, for pristine semiconductor surfaces, U^* does not necessarily coincide with V_{CPD} because of the variations in the surface potential induced by band bending [19]. To accurately analyze and interpret the experimental data, understanding the influence of the surface electronic properties on the U^* measurements is essential. However, the theoretical studies on this topic are limited.

In this study, we theoretically investigated the variation in U^* measured by KPFM on semiconductor surfaces, focusing on the influence of surface properties, particularly the strength of Fermi-level pinning. The pinning strength was modulated by introducing virtual surface states within the bandgap of the semiconductor sample and altering the density of states (DOS). Our calculations show that U^* depends not only on the presence or absence of surface states but also on their DOS. We found that when the Fermi-level pinning is either strong or negligibly weak, U^* corresponds to the difference in work functions between the probe tip and the semiconductor at the surface, which is directly related to the surface potential. By contrast, under moderate Fermi-level pinning conditions, U^* deviates from the value expected from the surface potential. Our findings suggest that U^* measured by KPFM on semiconductor surfaces cannot always be interpreted as a measure of the surface potential, thereby highlighting the significance of surface electronic properties for the accurate interpretation of KPFM data.

II. THEORETICAL COMPUTATION

To derive the theoretical U^* measured by KPFM, we numerically calculated the dependence of the electrostatic force (F_{elec}) between the tip and semiconductor sample on the bias voltage (U). For these computations, we employed the Poisson solver (SEMITIP) developed by Feenstra [20–25], which allowed us to calculate the electrostatic potential distribution in both the vacuum and semiconductor regions, induced by an applied potential from a metallic probe tip near the semiconductor surface. The electrostatic forces acting on the tip were calculated using the electric field and charge density on the tip surface, as derived from the potential distribution provided by the SEMITIP, as detailed in our previous work [26]. Subsequently, the bias voltage at which the electrostatic force was minimized was identified by fitting a ninth-order polynomial function to the calculated $F_{\mathrm{elec}}(U)$ spectra [9, 26]. As a model sample, we used an n-type GaAs(110) surface with a doping density of 5×10^{17} cm^{-3}, which has been extensively studied both theoretically and experimentally [9, 24, 27]. The pristine GaAs(110) surface has no surface states within the bandgap, resulting in a flat band from the bulk to the surface [19].

* ishida.nobuyuki@nims.go.jp

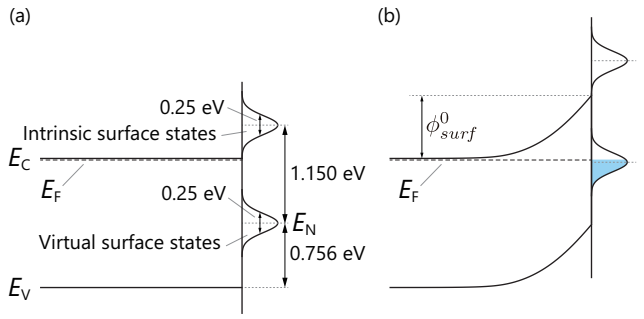

FIG. 1. (a) Schematic illustration of the band structure of the GaAs(110) surface used for the electrostatic force computation. Virtual surface states with a Gaussian-type energy distribution with a FWHM of 0.25 eV are introduced at the center of the bandgap. The CNL aligns with the centroid of the Gaussian distribution. In addition, the intrinsic surface states originated from the Ga dangling bond are incorporated above the conduction band edge. (b) shows the surface band bending induced by the occupation of the surface states above the CNL.

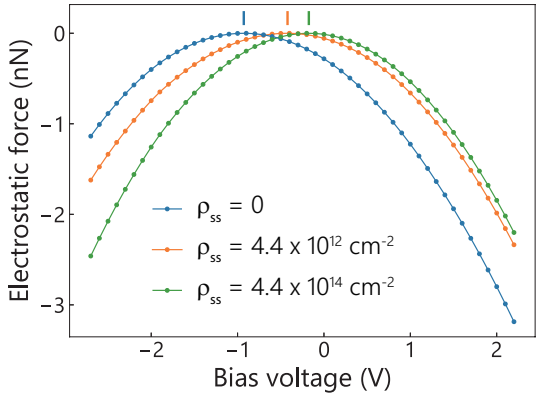

FIG. 2. $F_{\mathrm{elec}}(U)$ characteristics under ρ_{ss} of 0, 4.4×10^{12} cm^{-2}, and 4.4×10^{14} cm^{-2}. Vertical lines indicate the U^* for each ρ_{ss}.

To incorporate the effect of Fermi-level pinning into our simulation, we introduced virtual surface states within the bandgap of GaAs(110). The strength of Fermi-level pinning was controlled by varying the spatial density of the surface states ρ_{ss}. We assumed a Gaussian-type energy distribution with a full width at half maximum (FWHM) of 0.25 eV and positioned the centroid energy of the distribution at the center of the bandgap, as illustrated in Fig. 1(a). The charge neutrality level (CNL) E_{N} was aligned with the centroid energy of the Gaussian distribution. The CNL represents the energy below which the states are neutral when filled and positively charged when empty, and above which they are negatively charged when filled and neutral when empty [19]. We varied ρ_{ss} from 0 to 4.4×10^{14} cm^{-2}. A ρ_{ss} of zero corresponds to a pristine GaAs(110) surface. At a maximum value of 4.4×10^{14} cm^{-2}, which is equivalent to the spatial density of the Ga or As atoms on the GaAs(110) surface, the CNL of the surface states is strongly pinned at the Fermi level of the semiconductor, as discussed in Section III C.

In addition to the virtual surface states, we accounted for the intrinsic surface states originating from the Ga dangling bonds located above the conduction band edge (Fig. 1(a)). We assumed a Gaussian-type energy distribution with a FWHM of 0.25 eV. The centroid energy of the distribution was set to 1.150 eV above the CNL (Fig.1(a)) [24]. Although these surface states were included in our simulation because they have been experimentally observed on a pristine GaAs(110) surface [28], their inclusion did not influence the findings of this study.

Figure 1(b) illustrates the surface band bending induced by the occupation of the virtual surface states. When the band is flat, the virtual surface states are located below the Fermi level (Fig.1(a)), causing electrons in the conduction band near the surface to transition into the surface states. The occupation of the surface states above the CNL creates negative surface charges, initiating upward band bending near the surface to form a space charge layer, where dopant atoms are positively charged owing to electron depletion. This type of band bending occurs intrinsically at the surface under equilibrium conditions, even in the absence of a nearby probe tip. This differs from tip-induced band bending (TIBB). In this study, the magnitude of intrinsic band bending is denoted by ϕ^0_{surf} (Fig.1(b)). Note that the potential difference between the surface and far inside the bulk is generally referred to as the surface potential.

III. SIMULATION RESULTS

A. Bias dependence of electrostatic force

Figure 2 shows the $F_{\mathrm{elec}}(U)$ characteristics under ρ_{ss} values of 0, 4.4×10^{12}, and 4.4×10^{14} cm^{-2}. The direction of the force was configured such that a negative electrostatic force represents an attractive force. Vertical lines indicate U^* for each ρ_{ss}. The primary input parameters of the SEMITIP are the tip radius (R_{tip}), tip-sample separation (s), and work function difference between the tip and sample (V_{CPD}). We used parameter values of 10 nm, 1.53 nm, and -0.933 V for R_{tip}, s, and V_{CPD}, respectively. Note that the definition of V_{CPD} in SEMITIP differs slightly from ours. Thus, the actual input for V_{CPD} has the opposite sign (+0.933 V). These input parameters were determined by fitting the electrostatic-force simulation to the experimental data, as reported previously [26].

The $F_{\mathrm{elec}}(U)$ curves in Fig. 2 demonstrates that U^* varies depending not only on the presence or absence of virtual surface states within the bandgap but also on the magnitude of ρ_{ss}. On the pristine GaAs(110) surface ($\rho_{\mathrm{ss}} = 0$), where the band is flat up to the surface without

Fermi-level pinning, U^* (−0.931 V) was nearly identical to the input $V_{\rm CPD}$ (−0.933 V) used in the computations. Therefore, U^* agrees well with the quantity defined by

$$V_{\rm CPD} = \frac{W_{\rm sample} - W_{\rm tip}}{e}, \tag{1}$$

where $W_{\rm sample}$ and $W_{\rm tip}$ are the work functions of the sample and tip, respectively, and e is the elementary charge.

When $\rho_{\rm ss}$ was large (4.4×10^{14} cm^{-2}), the intrinsic band bending ($\phi^0_{\rm surf}$) was 0.756 eV, indicating that the surface band was pinned such that the Fermi level and CNL were nearly aligned, as shown in Fig. 1(b). In this situation, U^* (−0.175 V) deviates significantly from the input $V_{\rm CPD}$, instead closely matching the work function difference between the tip and the semiconductor at the surface (−0.177 V). The quantity $V^*_{\rm CPD}$ is expressed as:

$$V^*_{\rm CPD} = \frac{(W_{\rm sample} + \phi^0_{\rm surf}) - W_{\rm tip}}{e}, \tag{2}$$

where $W_{\rm sample} + \phi^0_{\rm surf}$ represents the work function of the surface ($W_{\rm surf}$). The relationships between the variables in Eq. 2 are shown in Fig. 3. This finding suggests that when the surface band is strongly pinned, KPFM is only sensitive to the potential at the surface, rather than being a weighted average of the potential near the surface. This indicates that KPFM is highly surface sensitive.

Although the high surface sensitivity of KPFM has been widely assumed, no theoretical verification has been performed for realistic tip-sample configurations, particularly for semiconductor samples. To address this, we examined the validity of this assumption under more general conditions, including measurements in ambient environments, where the values of s and $R_{\rm tip}$ tend to be larger. The electrostatic force calculations were performed with s varying from 1 to 100 nm and $R_{\rm tip}$ from 5 to 200 nm, as shown in Supplementary Fig. S1 [29]. In all cases, the magnitude of the electrostatic force and the curvature of the $F_{\rm elec}(U)$ spectra exhibited significant dependence on s and $R_{\rm tip}$. However, U^* remained nearly unchanged, with only minor fluctuations of approximately 1-2 mV. These findings indicate that the high surface sensitivity of KPFM is maintained across a broader range of conditions typically encountered in AFM/KPFM measurements.

For the pristine GaAs(110) surface described above, $\phi^0_{\rm surf}$ is zero, implying that the values of $V_{\rm CPD}$ and $V^*_{\rm CPD}$ are identical. Thus, when $\rho_{\rm ss}$ is both 0 and 4.4×10^{14} cm^{-2}, U^* obtained by KPFM can be considered as a measure of the physical quantity related to the surface potential, expressed in Eq. 2. This explains why KPFM is often described as a method for measuring surface potential.

By contrast, when $\rho_{\rm ss}$ was in the middle range (4.4×10^{12} cm^{-2}), corresponding to moderate Fermi-level pinning, U^* (−0.422 V) did not match with either $V_{\rm CPD}$ (−0.933 V) or $V^*_{\rm CPD}$ (−0.554 V). This finding suggests that the characterization of KPFM as a tool for measuring the surface potential is not entirely accurate. $\phi^0_{\rm surf}$ was 0.379 eV; however, $\phi^0_{\rm surf}$ estimated from U^* using Eq. 2 is 0.511 eV. This implies that the KPFM overestimates the surface band bending compared to the actual value.

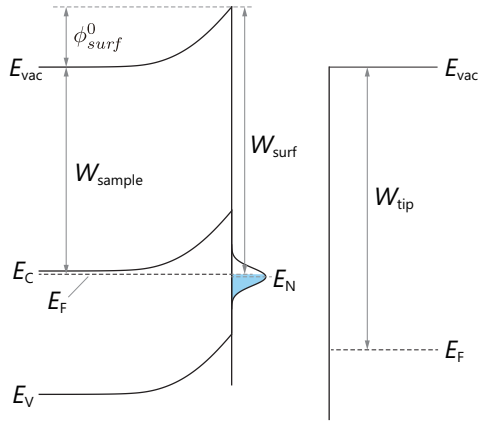

FIG. 3. Band structures of a metallic tip and a semiconductor sample prior to electrical connection. The vacuum level far inside the semiconductor is aligned with the vacuum level in the metallic tip. Surface band bending is caused by the occupation of virtual surface states, which is an intrinsic surface property irrespective of the presence of a nearby probe tip.

B. Discrepancy between U^* and $V^*_{\rm CPD}$

To analyze the deviation of U^* from $V^*_{\rm CPD}$ expressed in Eq. 2, the U^* and $V^*_{\rm CPD}$ values were calculated as functions of $\rho_{\rm ss}$, as shown in Fig. 4(a) as solid circles and triangles. The dashed horizontal line indicates the value of $V^*_{\rm CPD}$ for the pristine GaAs(110) surface. Figure 4(b) illustrates the difference between U^* and $V^*_{\rm CPD}$.

The variation in $V^*_{\rm CPD}$ (solid triangles) arises from changes in $\phi^0_{\rm surf}$ in Eq. 2, which reflects the degree of the surface band bending. For a small $\rho_{\rm ss}$, $V^*_{\rm CPD}$ is comparable to that of pristine GaAs(110) surface, indicating that the band is nearly flat up to the surface. As $\rho_{\rm ss}$ increases, the band gradually bends upward, and the bending saturates when the CNL aligns approximately with the Fermi level.

When $\rho_{\rm ss}$ was below 4.4×10^{11} cm^{-2} and above 4.4×10^{13} cm^{-2}, the difference between U^* and $V^*_{\rm CPD}$ was less than 20 mV. By contrast, when the spatial density of the surface states was in the ranges of 4.4×10^{11} cm^{-2} and 4.4×10^{13} cm^{-2}, U^* deviated from $V^*_{\rm CPD}$ by $>$ 20 mV. The largest deviation (132 mV) was observed at approximately 4.4×10^{12}cm^{-2}, with a steep decrease in the difference away from that point (Fig. 4(b)).

We also examined the generality of the results presented in this section for larger s and $R_{\rm tip}$, as shown in Supplementary Fig. S2[29]. In all cases, the dependence

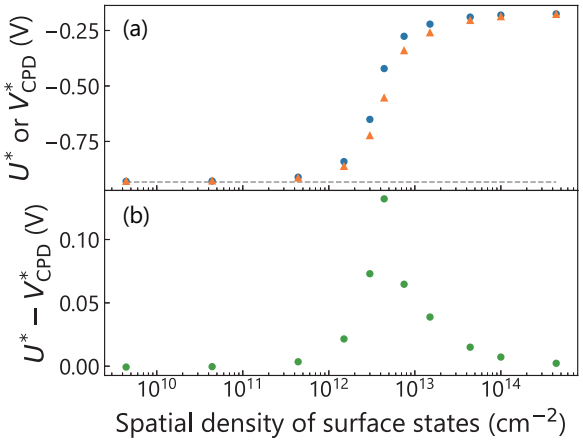

FIG. 4. (a) Solid circles and triangles represent U^* and V^*_{CPD} values, respectively, plotted as a function of ρ_{ss}. (b) shows the differences between U^* and V^*_{CPD} values.

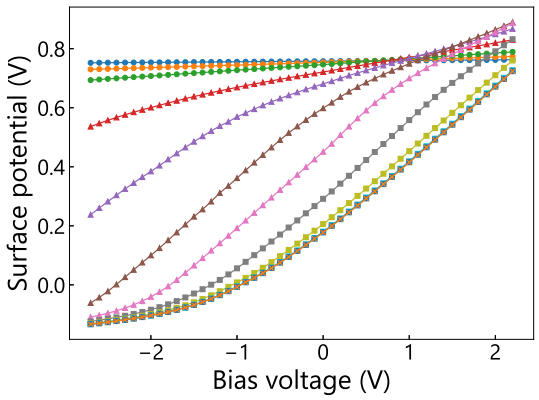

FIG. 5. Change in bias dependence of surface potentials ($\phi_{\mathrm{surf}}(U)$) depending on ρ_{ss}. The ρ_{ss} values are 0 (orange crosses), 4.4×10^9 (blue squares), 4.4×10^{10} (cyan squares), 4.4×10^{11} (olive squares), 1.5×10^{12} (gray squares), 3.0×10^{12} (pink triangles), 4.4×10^{12} (brown triangles), 7.5×10^{12} (purple triangles), 1.5×10^{13} (red triangles), 4.4×10^{13} (green circles), 1.0×10^{14} (orange circles), and 4.4×10^{14} (blue circles).

of U^* on the DOS of the surface states and its deviations from V^*_{CPD} closely resembled the trends observed in Fig. 4. These findings suggest that the discussions in the following sections are applicable to a broader range of conditions typically encountered in AFM/KPFM measurements.

C. Bias dependence of surface potential

To explore the correlation between U^* and the strength of Fermi-level pinning, we analyzed the bias dependence of the surface potential ($\phi_{\mathrm{surf}}(U)$) for each ρ_{ss} in Fig. 4, as shown in Fig. 5. Surface potential (or surface band bending) is defined as the electric potential difference between the surface and far inside the bulk (see Fig. 1(b)). On the pristine GaAs(110) surface, because ϕ^0_{surf} is zero, the observed variation in $\phi_{\mathrm{surf}}(U)$ can be attributed solely to TIBB. By contrast, in the presence of finite virtual surface states within the bandgap, $\phi_{\mathrm{surf}}(U)$ encompasses the contributions from both the TIBB and band bending caused by the occupation of the surface states.

For ρ_{ss} above 4.4×10^{13} cm^{-2} (solid circles), ϕ_{surf} remains relatively unchanged with the bias voltage, indicating strong Fermi-level pinning at the surface. Strong pinning implies that the surface states can accommodate sufficient charge to compensate for the charge on the tip surface. In other words, the line of electric force (or electric field) from the tip surface cannot penetrate the interior of the semiconductor, which suppresses the TIBB. This implies that the semiconductor surface behaves as a metallic surface. Under these conditions, the electrostatic force between the tip and the sample arises mostly from the Coulomb force between the charges on the tip surface and the charges in the surface states (hereinafter referred to as surface charge).

By contrast, for ρ_{ss} below 4.4×10^{11} cm^{-2} (solid squares), the curves exhibit bias dependences similar to those of pristine GaAs(110) (orange crosses). This suggests that surface charges play little role in preventing the penetration of the line of electric force into the semiconductor. In this case, charges generated near the surface owing to TIBB (accumulated carriers or charged dopant atoms created by carrier depletion, hereinafter referred to as bulk charge) predominantly contribute to compensating for the charges on the tip surface. Therefore, the electrostatic force between the tip and sample is mostly caused by charges on the tip surface and bulk charges near the surface.

When ρ_{ss} fell within the middle range, ranging from 4.4×10^{11} to 4.4×10^{13} cm^{-2} (solid triangles), ϕ_{surf} exhibited significant variations with the bias voltage, indicating relatively weak Fermi-level pinning. Nonetheless, the curve shapes display different bias dependencies compared to the one observed for pristine GaAs(110) (orange crosses). These characteristics suggest that although surface charges contribute to shielding the electric field to some extent, the amount is insufficient to entirely impede the penetration of the electric field into the semiconductor. In this case, both the surface and bulk charges contribute substantially to the electrostatic force acting between the tip and sample. The ratio of the contributions of these two charge types is considered to vary depending on ρ_{ss}.

IV. DISCUSSION

The results discussed thus far indicate that when the electrostatic force between the tip and the sample arises primarily from either surface charges or bulk charges, U^*

measured by KPFM can be interpreted as a measure of the physical quantity related to the surface potential, as expressed in Eq. 2. By contrast, when the electrostatic force originates substantially from both the surface and bulk charges, strictly speaking, KPFM cannot be described as a tool for measuring the surface potential.

When both surface and bulk charges contribute to the electrostatic force, one might intuitively expect U^* (or CPD) to reflect the electric potential at both the surface and the bulk near the surface, that is, a weighted average of the electric potential in the region where band bending occurs. If this were the case, KPFM would underestimate the magnitude of the band bending (or surface potential). However, as discussed in Section II, U^* is observed to be larger than V^*_{CPD}, indicating that band bending is overestimated.

The underlying cause of this overestimation remains unclear. However, one possible explanation is as follows. During bias application, the electrostatic force between the charges on the tip surface and surface charges is minimized when the CNL (or surface Fermi level) aligns with the the Fermi level of the tip. On the contrary, the electrostatic force between the charges on the tip surface and bulk charges reaches its minimum when the Fermi level of the semiconductor in the bulk aligns with the Fermi level of the tip. Under moderate Fermi-level pinning conditions, the interplay between the two effects determines U^* based on the relative amounts of surface and bulk charges, and the value is expected to correspond to V^*_{CPD}. However, in KPFM measurements, the surface charges are much closer to the tip surface than the bulk charges, and their contribution to the electrostatic force is therefore expected to be significantly larger. Consequently, the surface potential measured by KPFM becomes larger than the intrinsic surface potential, resulting in an overestimation of the band bending.

Finally, we discuss the relationship between our findings and the actual KPFM measurements. KPFM experiments are frequently performed on devices and materials under ambient conditions. In such environments, strong Fermi-level pinning frequently occurs because of the surface states within the bandgap, which are induced by factors such as surface reconstruction, oxidation, and contamination. Therefore, the measured CPD values are expected to correspond to the quantities represented by Eq. 2. However, it is important to note that directly analyzing the work function of samples remains challenging because the magnitude of band bending (surface potential) is generally unknown. Nonetheless, when measuring changes in CPD induced by external stimuli, such as an applied bias voltage or light irradiation, quantitative analysis of the variation in the electric potential is feasible, provided that the surface pinning position remains unchanged [5, 11].

When performing measurements on surfaces with low surface energy that remain clean, even under ambient conditions, or on clean surfaces prepared in ultrahigh vacuum, careful analysis of the experimental data may be required. For example, if surface steps introduce surface states within the bandgap, the strength of the Fermi-level pinning gradually weakens as the distance from the steps increases. In the middle of such regions, the CPD measured by KPFM may deviate from V^*_{CPD} in Eq. 2, because of the interplay between the surface and bulk charges. This necessitates caution when performing precise quantitative comparisons between experimental data and theoretical models.

V. CONCLUSION

We utilized a theoretical simulation of the electrostatic force acting between the probe tip and the semiconductor sample to investigate the influence of Fermi-level pinning on CPD measurements via KPFM. The strength of the Fermi-level pinning was controlled by introducing virtual surface states within the semiconductor bandgap and varying the DOS. In cases where the Fermi-level pinning is negligibly weak or strong, such that the surface band bending remains nearly invariant under an applied bias, KPFM was found to measure quantities directly related to the surface potential. This finding indicated that KPFM is highly surface sensitive. By contrast, when moderate Fermi-level pinning occurred, the CPD values deviated from those predicted based on the surface potential. Under these conditions, both the surface and bulk charges in the semiconductor contributed to the electrostatic force between the tip and sample. The cause of the deviations was inferred to arise from larger contribution of the surface charges to the electrostatic force than the bulk charges due to their proximity to the tip surface. Although such situations are not frequently encountered in typical KPFM experiments, care may be required when performing measurements on clean surfaces prepared under ultrahigh-vacuum conditions and making detailed quantitative comparisons with theoretical models.

ACKNOWLEDGMENTS

This study was partially supported by JSPS KAKENHI Grant Numbers JP17K06366, JP21H01818, and 24K01367.

[1] M. Nonnenmacher, M. P. O'Boyle, and H. K. Wickramasinghe, Kelvin probe force microscopy, Appl. Phys. Lett. **58**, 2921 (1991).

[2] S. Sadewasser and T. Glatzel, eds., *Kelvin Probe Force Microscopy: Measuring and Compensating Electrostatic Forces* (Springer, 2012).

[3] R. Shikler, T. Meoded, N. Fried, and Y. Rosenwaks, Potential imaging of operating light-emitting devices using Kelvin force microscopy, Appl. Phys. Lett. **74**, 2972 (1999).

[4] T. Glatzel, S. Sadewasser, R. Shikler, Y. Rosenwaks, and M. C. Lux-Steiner, Kelvin probe force microscopy on iii-v semiconductors: the effect of surface defects on the local work function, Mater. Sci. Eng. B **102**, 138 (2003).

[5] M. Cai, N. Ishida, X. Li, X. Yang, T. Noda, Y. Wu, F. Xie, H. Naito, D. Fujita, and L. Han, Control of electrical potential distribution for high-performance perovskite solar cells, Joule **2**, 296 (2018).

[6] T. Noda, N. Ishida, T. Mano, and D. Fujita, Direct observation of charge accumulation in quantum well solar cells by cross-sectional Kelvin probe force microscopy, Appl. Phys. Lett. **116**, 163501 (2020).

[7] T. Nakamura, N. Ishida, K. Sagisaka, and Y. Koide, Surface potential imaging and characterizations of a gan p-n junction with Kelvin probe force microscopy, AIP Adv. **10**, 085010 (2020).

[8] M. Hiraoka, N. Ishida, A. Matsushita, R. Uchida, T. Sekimoto, T. Yamamoto, T. Matsui, Y. Kaneko, K. Miyano, M. Yanagida, and Y. Shirai, Degradation of perovskite photovoltaics manifested in the cross-sectional potential profile studied by quantitative Kelvin probe force microscopy, ACS Appl. Ener. Mater. **5**, 4232 (2022).

[9] N. Ishida and T. Mano, Quantitative characterization of built-in potential profile across gaas p-n junctions using Kelvin probe force microscopy with qPlus sensor AFM., Nanotechnology **35**, 065708 (2024).

[10] S. Y. Luchkin, H.-Y. Amanieu, D. Rosato, and A. L. Kholkin, Li distribution in graphite anodes: A Kelvin probe force microscopy approach, J. Power Sources **268**, 887 (2014).

[11] H. Masuda, N. Ishida, Y. Ogata, D. Ito, and D. Fujita, Internal potential mapping of charged solid-state-lithium ion batteries using in situ Kelvin probe force microscopy, Nanoscale **9**, 893 (2017).

[12] H. Masuda, K. Matsushita, D. Ito, D. Fujita, and N. Ishida, Dynamically visualizing battery reactions by operando Kelvin probe force microscopy, Commun. Chem. **2**, 140 (2019).

[13] M. Otoyama, T. Yamaoka, H. Ito, Y. Inagi, A. Sakuda, M. Tatsumisago, and A. Hayashi, Visualizing local electrical properties of composite electrodes in sulfide all-solid-state batteries by scanning probe microscopy, J. Phys. Chem. C **125**, 2841 (2021).

[14] N. Ishida, Utilizing the surface potential of a solid electrolyte region as the potential reference in Kelvin probe force microscopy, Beilstein J. Nanotechnol. **13**, 1558 (2022).

[15] N. Ishida, Local impedance measurement by direct detection of oscillating electrostatic potential using Kelvin probe force microscopy, J. Phys. Chem. C **126**, 17627 (2022).

[16] International Union of Pure and Applied Chemistry. Compendium of Chemical Terminology: IUPAC Gold Book. Accessed May, 2024 , `https://goldbook.iupac.org/terms/view/C01293`.

[17] T. Beierlein, W. Brütting, H. Riel, E. Haskal, P. Müller, and W. Rieß, Kelvin probe investigations of metal work functions and correlation to device performance of organic light-emitting devices, Synthetic Metals **111-112**, 295 (2000).

[18] P. A. Fernández Garrillo, B. Grévin, N. Chevalier, and L. Borowik, Calibrated work function mapping by Kelvin probe force microscopy, Rev. Sci. Instrum. **89**, 043702 (2018).

[19] W. Mönch, *Semiconductor Surfaces and Interfaces, Third edition* (Springer, 2001).

[20] R. M. Feenstra, Electrostatic potential for a hyperbolic probe tip near a semiconductor, J. Vac. Sci. Technol. B **21**, 2080 (2003).

[21] R. M. Feenstra, S. Gaan, G. Meyer, and K. H. Rieder, Low-temperature tunneling spectroscopy of Ge(111)c(2×8) surfaces, Phys. Rev. B **71**, 125316 (2005).

[22] R. M. Feenstra, Y. Dong, M. P. Semtsiv, and W. T. Masselink, Influence of tip-induced band bending on tunnelling spectra of semiconductor surfaces, Nanotechnology **18**, 044015 (2006).

[23] Y. Dong, R. M. Feenstra, M. P. Semtsiv, and W. T. Masselink, Band offsets of InGaP/GaAs heterojunctions by scanning tunneling spectroscopy, J. Appl. Phys. **103**, 073704 (2008).

[24] N. Ishida, K. Sueoka, and R. M. Feenstra, Influence of surface states on tunneling spectra of n-type GaAs(110) surfaces, Phys. Rev. B **80**, 075320 (2009).

[25] S. Gaan, G. He, R. M. Feenstra, J. Walker, and E. Towe, Size, shape, composition, and electronic properties of InAs/GaAs quantum dots by scanning tunneling microscopy and spectroscopy, J. Appl. Phys. **108**, 114315 (2010).

[26] N. Ishida and T. Mano, Quantitative theoretical analysis of the electrostatic force between a metallic tip and semiconductor surface in Kelvin probe force microscopy, Nanotechnology **36**, 075701 (2025).

[27] R. M. Feenstra, Tunneling spectroscopy of the (110) surface of direct-gap III-V semiconductors, Phys. Rev. B **50**, 4561 (1994).

[28] D. Straub, M. Skibowski, and F. J. Himpsel, Conduction-band dispersion, critical points, and unoccupied surface states on GaAs(110): A high-resolution angle-resolved inverse photoemission study, Phys. Rev. B **32**, 5237 (1985).

[29] See Supplemental Material at [URL] for the calculations of $F_{\mathrm{elec}}(U)$ spectra with large s and R_{tip}; the calculations of U^* and V^*_{CPD} as functions of ρ_{ss} for large s and R_{tip}.